Mixed-Mode Dynamic Crack Growth in a Functionally Graded Particulate Composite: Experimental Measurements and Finite Element Simulations

Madhu Kirugulige
The Goodyear Tire and Rubber Company,
Department of Mechanical Engineering,
Auburn University,
Auburn, AL 36849

Hareesh V. Tippur
Alumni Professor
Fellow ASME
Department of Mechanical Engineering,
Auburn University,
Auburn, AL 36849

Mixed-mode dynamic crack growth behavior in a compositionally graded particle filled polymer is studied experimentally and computationally. Beams with single edge cracks initially aligned in the direction of the compositional gradient and subjected to one-point eccentric impact loading are examined. Optical interferometry along with high-speed photography is used to measure surface deformations around the crack tip. Two configurations, one with a crack on the stiffer side of a graded sheet and the second with a crack on the compliant side, are tested. The observed crack paths are distinctly different for these two configurations. Furthermore, the crack speed and stress intensity factor variations between the two configurations show significant differences. The optical measurements are examined with the aid of crack-tip fields, which incorporate local elastic modulus variations. To understand the role of material gradation on the observed crack paths, finite element models with cohesive elements are developed. A user-defined element subroutine for cohesive elements based on a bilinear traction-separation law is developed and implemented in a structural analysis environment. The necessary spatial variation of material properties is introduced into the continuum elements by first performing a thermal analysis and then by prescribing material properties as temperature dependent quantities. The simulated crack paths and crack speeds are found to be in qualitative agreement with the observed ones. The simulations also reveal differences in the energy dissipation in the two functionally graded material (FGM) cases. T-stresses and hence the crack-tip constraint are significantly different. Prior to crack initiation, larger negative T-stresses near the crack tip are seen when the crack is situated on the compliant side of the FGM. [DOI: 10.1115/1.2932095]

1 Introduction

Functionally graded materials (FGMs) are a new class of materials having continuous spatial variation of properties (mechanical, thermal, piezoelectric, etc.). Generally, they are multiphase materials having continuously varying volume fractions of constituent phases along a desired spatial direction. Typical applications of FGM include thermal barrier coatings in high temperature components, impact resistant structures for armors and ballistics, interlayers in microelectronic packages, etc. The study of dynamic failure of FGM is essential in order to design structures involving these novel materials for elevated rates of loading. For example, Kirugulige et al. [1] have experimentally demonstrated (under Mode-I impact loading) that functionally graded sandwich structures perform better compared to their conventional counterparts at least in two respects. The face-sheet/core delamination can be mitigated by using a graded interfacial architecture in place of a conventional one. Also, the crack initiation can be delayed in the former when compared to the latter. Since a crack and/or loading directions can be inclined to the direction of material gradation in a FGM, fracture generally will be mixed mode in nature (say, Modes I and II). Therefore, it is important to understand the role spatial variation of properties has on the crack path under stress wave loading conditions.

The work of Delale and Erdogan [2] is among of the early studies on fracture behavior of FGM, where they have shown that stress intensity factors in nonhomogeneous materials are affected by compositional gradients even though the inverse $\sqrt{r}$ singularity is preserved near the crack tip. In a later work, Konda and Erdogan [3] have provided the expressions for stress intensity factors (SIFs) of a mixed-mode quasistatic fracture problem in nonhomogeneous materials. In the past few years, Shukla and coworkers [4,5] have reported crack-tip stress fields for dynamically growing cracks in FGM for Mode-I and mixed-mode loading conditions. There are relatively few experimental methods available to study mixed-mode dynamic fracture and measure fracture parameters. Butcher et al. [6] have demonstrated the feasibility of using optical interferometry to study fracture behavior of glass-filled epoxy FGM beams. Rousseau and Tippur [7] have reported on the role of material gradation on crack kinking under quasistatic conditions. They have also examined the effect of material gradation on Mode-I dynamic fracture in a separate study [8]. Kirugulige and Tippur [9] have conducted mixed-mode dynamic fracture experiments on FGM samples made of compositionally graded glass-filled epoxy sheets with edge cracks initially along the gradients. In that work [9], the authors have observed that when a crack is situated on the compliant side of the sample, it kinks significantly less compared to when it is on the stiffer side when impact loaded in eccentric one-point loading configuration. In order to further understand the role of material grading on ensuing crack paths, these experiments are reexamined here with

Contributed by the Applied Mechanics Division of ASME for publication in the JOURNAL OF APPLIED MECHANICS. Manuscript received May 24, 2007; final manuscript received February 7, 2008; published online July 10, 2008. Review conducted by Marek-Jerzy Pindera.

the aid of crack-tip fields for nonhomogeneous materials along with a complementary numerical investigation of the problem.

The numerical simulation of crack growth during mixed-mode dynamic fracture events is computationally challenging when compared to Mode-I counterparts. It is also more complex in case of FGM because mode mixity arises not only from geometrical and loading configurations but also from the material nonhomogeneity parameter. In order to predict the crack kinking direction in a FGM, the numerical scheme should be able to represent spatial variation of material properties and the evolution of crack path must be a natural outcome of the analysis. There are mainly three different approaches within the framework of finite element method to simulate this problem. The first is an automated moving finite element approach with local remeshing along the crack path. This approach requires a user-defined crack increment and relies on one of the mixed-mode fracture criteria for determining crack growth direction. Bittencourt et al. [10] and Nishioka [11] have successfully used this approach to simulate mixed-mode crack propagation in homogeneous materials. Nishioka et al. [12] were able to predict the crack path of a mixed-mode dynamic fracture experiment using moving singular finite element method based on Delaunay automatic mesh generation. In a comprehensive numerical work on mixed-mode crack growth simulations including FGM, Kim and Paulino [13] have used local remeshing technique to predict the crack path of mixed-mode quasistatic fracture tests of Rousseau and Tippur [7]. Recently, Tilbrook et al. [14] have simulated quasistatic crack propagation in FGMs under flexural loading conditions. The aforementioned approaches require a robust automatic remeshing algorithm, an elaborate bookkeeping system of node numbering to readjust the mesh pattern periodically, and a mesh rezoning procedure for mapping the solution fields of the previous mesh onto those in the current mesh.

The second approach is to use cohesive elements with the conceptual underpinnings found in the works of Dugdale [15] and Barenblatt [16]. There are two basic types of cohesive zone modeling approaches – intrinsic and extrinsic – methods. The former is characterized by its hardening and softening portions of the traction-separation law (TSL), whereas the latter has only the softening portion. The intrinsic cohesive element formulation in the context of finite element method was proposed early on by Needleman [17]. Numerous other investigators have used the intrinsic type of formulation with different shapes of TSL: exponential [18–21], bilinear [21–24], and trapezoidal [25,26] types. Xu and Needleman [18] have performed mixed-mode dynamic crack growth simulations in brittle solids. Wang and Nakamura [19] have used an exponential TSL to simulate dynamic crack propagation in elastic-plastic FGMs. The applicability of exponential and bilinear types of cohesive zone models to modified boundary layer analysis was conducted by Shim et al. [21]. Mode-I and mixed-mode dynamic fracture simulations in FGM have been reported by Zhang and Paulino [24]. Madhusudhana and Narasimhan [26] have used a trapezoidal TSL to simulate mixed-mode crack growth in ductile adhesive joints. The extrinsic type of formulation has also been used by many researchers [27,28].

Recently, Belytschko and co-workers [29,30] have proposed a third method called the extended finite element method (XFEM) to model arbitrary discontinuities in finite element meshes. In this method, discontinuous enrichment functions are added to the finite element approximation to account for the presence of a crack while preserving the classical displacement variational setting. This flexibility enables the method to simulate crack growth without remeshing.

Physical mechanisms governing dynamic crack propagation in FGM under mixed-mode loading are not clearly understood. Observations based on the study of quasistatic fracture indicate that under mixed-mode loading, the crack tends to grow according to a locally Mode-I dominated condition as predicted in the $K_{II}=0$ criterion or the maximum tensile stress criterion criterion [31]. Extending these methods to dynamic mixed-mode fracture of FGM requires evaluation of one of the fracture criterion and local remeshing. However, cohesive elements allow crack initiation and kinking to occur without the need for defining the crack path a priori. Therefore, in the current work, intrinsic cohesive element method with bilinear TSL is used to model dynamic mixed-mode crack growth in FGM. In order to implement this in the context of finite element analysis, a user subroutine is developed and augmented with ABAQUS™ (Version 6.5). The spatial variation of material properties in continuum elements is incorporated by conducting a thermal analysis and then applying temperature dependent material properties. The spatial variation of dynamic initiation toughness obtained by Mode-I dynamic fracture tests on homogeneous samples of different volume fractions of the filler material is also incorporated. The mixed-mode stress intensity factor histories up to crack initiation are computed by regression analyses of crack opening and sliding displacements. The simulated crack paths are found to be in qualitative agreement with the experimentally observed ones.

2 Experimental Details

In this section, we summarize the main experimental features and relevant results to the current work. Additional details can be found elsewhere [9].

2.1 Material Preparation and Test Configuration. FGM samples were prepared by continuously varying the volume fraction of solid glass filler particles (35 μm mean diameter) in an epoxy matrix. The gravity assisted casting method [6] was used to produce a monotonic variation of volume fraction of glass particles in the vertical direction of a cast sheet. A schematic of the specimen is shown in Fig. 1(*a*), where the gray scale is used to represent the compositional gradation. The elastic modulus and Poisson's ratio were estimated by measuring the elastic wave speeds in the cast sheet at several discrete locations using the ultrasonic pulse-echo method. The variations of elastic modulus and mass density along the width of a sample are shown in Fig. 1(*b*). The elastic modulus varies from $\sim$10 GPa to $\sim$4 GPa over a width of $\sim$43 mm. The mass density varies from $\sim$1750 kg/m^3 to $\sim$1175 kg/m^3 over the same width. The corresponding variation in Poisson's ratio was 0.33–0.37.

In cohesive element models, the fracture energy is an important input parameter, which has to be determined experimentally. To this end, Mode-I crack initiation toughness tests were conducted on *homogeneous* edge cracked beam samples of various volume fractions of the filler. Dally–Sanford single strain gage method [32] was used to record strain history in each case and was, in turn, used to obtain Mode-I crack initiation toughness (see Ref. [33] for details). Figure 1(*c*) shows the variation of the local Mode-I crack initiation toughness (K_{ICR}) as a function of position inferred from these tests. A monotonic increase in crack initiation toughness values can be seen at lower values of E and hence lower volume fraction of the filler. An increase in fracture toughness by a factor of $\sim$1.5 occurs when the filler volume fraction increases from 0% to 40% with a corresponding change in the elastic modulus by a factor of $\sim$2.4.

Mixed-mode fracture experiments were conducted on FGM samples in two separate configurations: (a) an edge crack on the compliant side of the sample with an impact on the stiffer side, and (b) an edge crack on the stiffer side of the sample with an impact on the compliant side. These configurations are shown schematically in Fig. 2. The specimens were impacted using a pneumatic hammer with a velocity of $\sim$5 m/s at an offset distance of 25.4 mm with respect to the initial crack orientation in both configurations. Here, the elastic modulus at the edge of the cracked sheet, behind the crack tip, is denoted by E_1 and the one ahead of the crack tip as E_2. With this notation, henceforth, Type-(a) experiments are denoted as $E_1 < E_2$ and Type-(b) experiments as $E_1 > E_2$. Except for this reversal of compositional gradient, all other conditions were the same for both cases. The coherent gra-

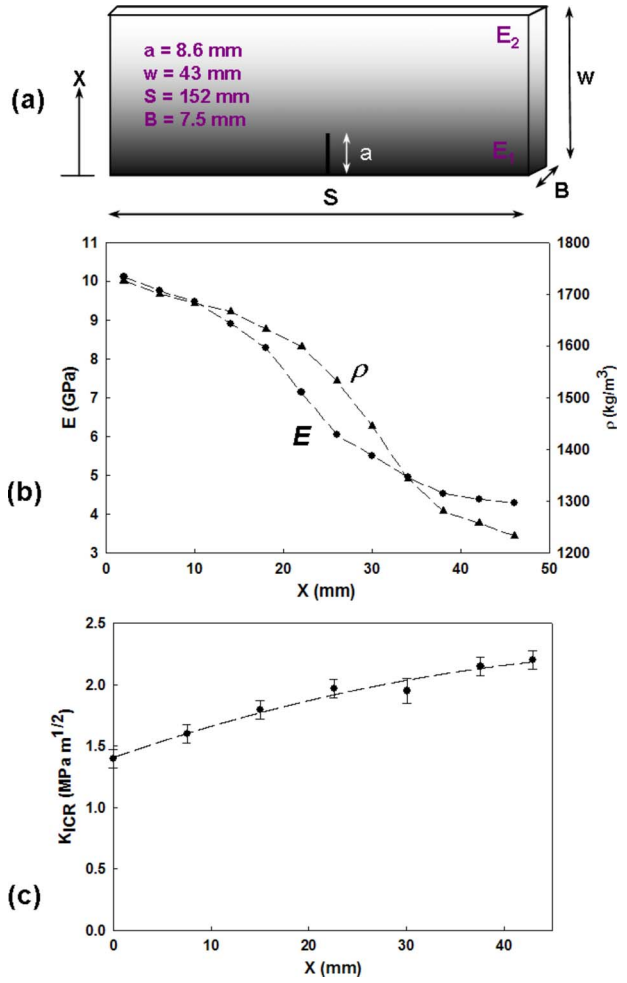

Fig. 1 (*a*) **Schematic of the FGM specimen (darker shades represent stiffer materials), (*b*) material property variation along the width of the sample, and (*c*) variation of dynamic crack initiation toughness along the width of the sample**

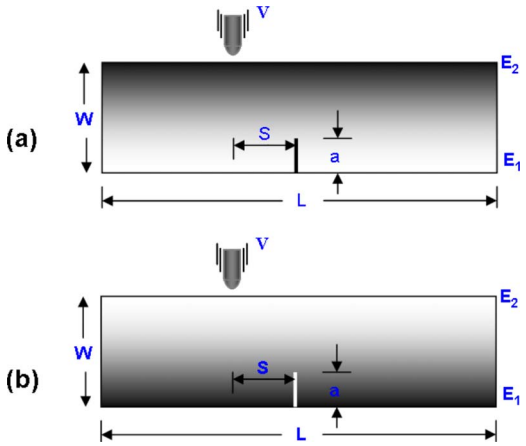

Fig. 2 Two mixed-mode FGM test configurations: (*a*) crack on the compliant side of the sample with impact occurring on the stiff side ($E_1 < E_2$) and (*b*) crack on the stiff side of the sample with impact occurring on the compliant side ($E_1 > E_2$). Impact velocity (V)=5 m/s. (Shading is used to denote compositional gradation; darker shades represent stiffer material.)

dient sensing (CGS) [34] method was used in conjunction with high-speed photography to measure instantaneous surface deformations around the crack tip. Specifically, angular deflections of the light rays proportional to $\partial w/\partial X_1$ (w being the out-of-plane displacement and X_1 is the initial crack orientation direction) were measured in the crack-tip vicinity as interference fringes. A framing rate of 200,000 was used and images were recorded at 5 μs intervals. A complete fracture of the specimen typically occurred after about 220 μs. Representative interferograms for both FGM configurations (one from the preinitiation and one from the postinitiation period) are shown in Fig. 3. Under the assumption of plane stress condition, out-of-plane displacement w can be related to the sum of the in-plane stresses $(\sigma_x+\sigma_y)$ using elastic constants.

2.2 Experimental Results: Crack Path History. Multiple experiments were conducted for both the FGM specimen configurations $E_1 < E_2$ and $E_1 > E_2$ to ensure repeatability. Four fractured samples from each configuration are shown in Figs. 4(*a*) and 4(*b*). A high degree of reproducibility in crack paths is clearly evident. More importantly, a distinctly different crack path can be seen in these two configurations. Figure 4(*c*) shows photographs of the fractured specimens for one representative experiment in each configuration. The impact point is located on the top edge of each image and the initial crack tip is at the bottom edge as indicated. The reflective area on each specimen surface is the region of interest where surface deformations were monitored optically. The crack was situated on the compliant side in Fig. 4(*c*) and on the stiffer side in Fig. 4(*d*). The difference in crack paths in the lower half of the specimen after initiation is quite striking in these images. For the case of $E_1 < E_2$, crack growth occurs in a near Mode-I fashion with an initial kink angle of $\phi \sim 4$ deg with respect to the X_1-axis whereas for the case $E_1 > E_2$, the crack growth occurs at an initial kink angle of $\phi \sim 16$ deg. Subsequent crack growth in the case of $E_1 < E_2$ shows a tendency for the crack to grow nearly along the X_1-direction. On the other hand, in the case of $E_1 > E_2$, the crack growth is essentially self-similar following initiation with a continued growth at an angle of $\sim$16 deg with respect to the X_1-direction. In the upper half of the sample, the crack growth is affected by a combination of free-edge and impact point interactions. Therefore, in the current work, the simulation results are compared with the experimental ones on initial crack growth in both configurations.

3 Evaluation of Stress Intensity Factors

The elastic crack-tip fields are available for nonhomogeneous materials having exponential variation of material properties. The use of exponential variation simplifies the process of deriving the crack-tip fields. However, processing a FGM having an exponential variation of elastic modulus is difficult. Recently, attempts have been made to derive crack-tip stress fields for a FGM with a linear variation of elastic modulus [35]. For an edge cracked beam having a linear material property, variation along the X_1-direction is described by the equation

$$E(X_1) = E_0(1 + \delta_f X_1) = E_0(1 + \alpha X_1' + \beta X_2') \tag{1}$$

where E_0 is the elastic modulus at the crack tip as shown in Fig. 5(*a*), and the parameters α and β are related to the nonhomogeneity parameter δ_f as

$$\alpha = \delta_f \cos\phi, \quad \beta = \delta_f \sin\phi \tag{2}$$

where ϕ is the crack kink angle. For a Mode-I crack propagation, ϕ=0, $\alpha = \delta_f$, and the axes X_1–X_2 and X_1'–X_2' coincide. (In the current work, X_1 varies in the range $-0.0085\ \text{m} \leq X_1 \leq 0.0345$ m.) The spatial variation of elastic modulus is approximated as a linear function (Fig. 5(*b*)) for both the FGM configurations. A four-term expansion for the sum of in-plane stresses $(\sigma_x+\sigma_y)$ is deduced from Eqs. (31) and (32) of Ref. [35] as

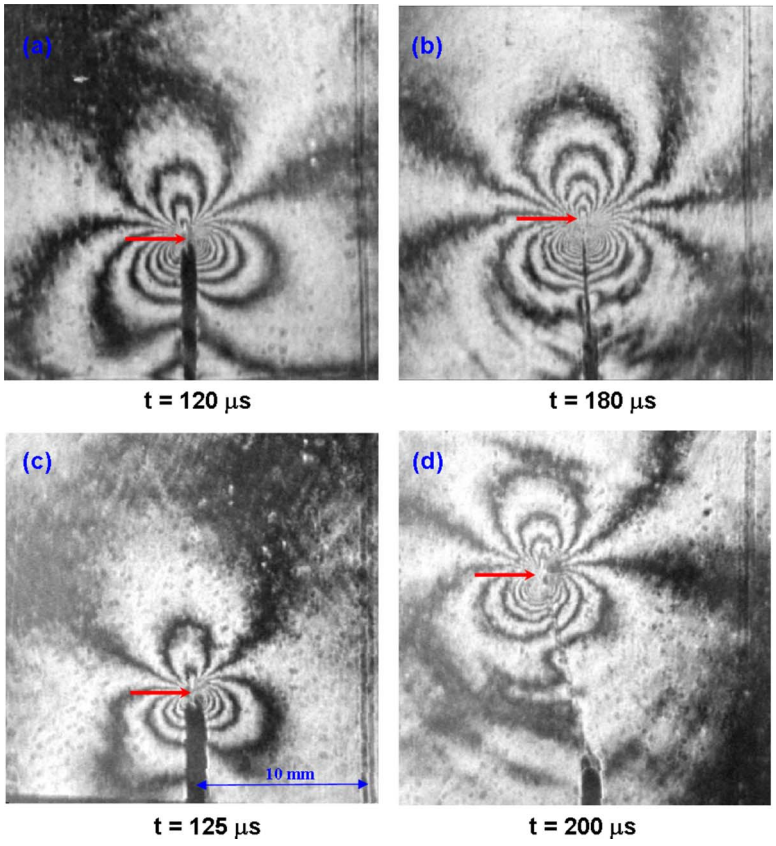

Fig. 3 Selected CGS interferograms representing contours of $\delta w/\delta X_1$ in FGM samples; (*a*) and (*b*) are for the case of $E_1 < E_2$ and (*c*) and (*d*) are for the case of $E_1 > E_2$. The time at which the images are taken after impact is indicated below each image. The current crack tip is indicated by an arrow.

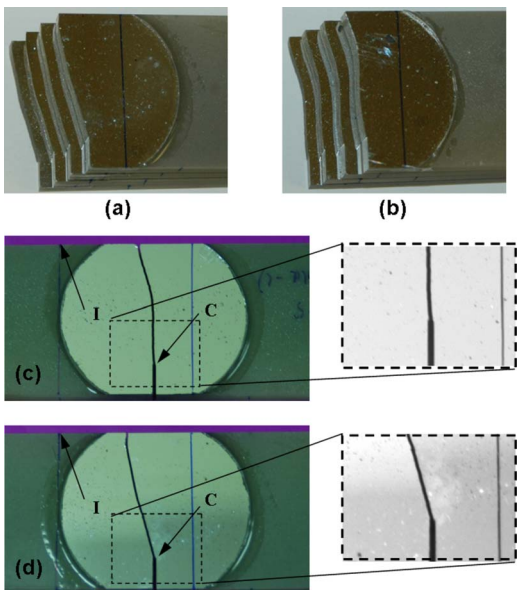

Fig. 4 Multiple fractured FGM specimens (right half) demonstrating experimental repeatability for (*a*) FGM with a crack on the stiffer side ($E_1 < E_2$) and (*b*) FGM with a crack on the compliant side ($E_1 > E_2$). Photograph showing fractured specimens for (*c*) FGM with a crack on the compliant side ($E_1 < E_2$) and (*d*) FGM with a crack on the stiffer side ($E_1 > E_2$). Impact point is indicated by letter "I" and initial crack tip by letter "C."

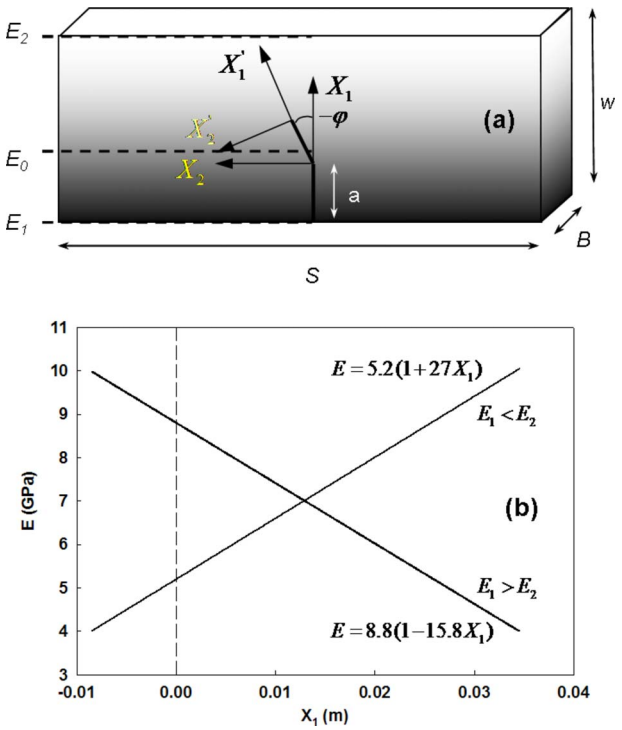

Fig. 5 (*a*) Schematic of FGM sample with linear material property variation, and (*b*) elastic modulus variation in graded samples (broken line denotes the crack tip location)

$$\sigma_x+\sigma_y=2\left[A_0(t)r^{-1/2}\cos\frac{\theta}{2}-C_0(t)r^{-1/2}\sin\frac{\theta}{2}+B_0(t)+A_1(t)r^{1/2}\cos\frac{\theta}{2}+C_1(t)r^{1/2}\sin\frac{\theta}{2}+B_1(t)r\cos\theta+D_1(t)r\sin\theta\right]$$
$$+\alpha\left[A_0(t)r^{1/2}\left\{-2\sin\theta\sin\frac{\theta}{2}-2\cos\frac{\theta}{2}\right\}+C_0(t)r^{1/2}\left\{-2\sin\theta\cos\frac{\theta}{2}-2\sin\frac{\theta}{2}\right\}-B_0(t)r\cos\theta-2D_0(t)r\sin\theta\right]$$
$$+\beta\left[A_0(t)r^{1/2}\left\{2\sin\theta\cos\frac{\theta}{2}+2\sin\frac{\theta}{2}\right\}+C_0(t)r^{1/2}\left\{-2\sin\theta\sin\frac{\theta}{2}-2\cos\frac{\theta}{2}\right\}+3B_0(t)r\sin\theta-D_0(t)r\cos\theta\right] \quad (3)$$

In the above equation, r and θ are the crack-tip coordinates instantaneously aligned with the current crack tip. The mixed-mode stress intensity factors, K_I and K_{II} are related to the constants of the singular terms in the above equation as $K_I(t)=A_0(t)\sqrt{2\pi}$ and $K_{II}(t)=C_0(t)\sqrt{2\pi}$. As already mentioned, the CGS fringes represent surface slopes in the principal direction of the grating (in the current work, the direction of initial crack orientation). These surface slopes can be related to the corresponding fringe orders N by using a difference approximation,

$$\frac{\partial w}{\partial X_1}\approx\frac{\delta w}{\delta X_1}=\frac{w_{i+1}-w_i}{\delta X_1}=\frac{Np}{2\Delta} \quad (4)$$

where δ represents the difference operator, p is the pitch of the grating, and Δ is the grating separation distance. By substituting the expression for the out-of-plane displacement w under plane stress assumption,

$$\frac{-\nu B}{2\delta X_1}\left[\left(\frac{\sigma_x+\sigma_y}{E_0(1+\alpha X_1'+\beta X_2')}\right)_{i+1}-\left(\frac{\sigma_x+\sigma_y}{E_0(1+\alpha X_1'+\beta X_2')}\right)_i\right]=\frac{Np}{2\Delta} \quad (5)$$

where B is the specimen thickness and ν is Poisson's ratio of the material. Furthermore, δX_1 denotes shearing distance ($\sim$1.05 mm in the current experimental setup). In the above equation, $\sigma_x+\sigma_y$ is substituted from Eq. (3) with r and θ being evaluated at locations denoted by i and $i+1$ as

$$r_i=\sqrt{X_1^2+X_2^2},\quad \theta_i=\tan^{-1}\frac{X_2}{X_1}$$
$$r_{i+1}=\sqrt{(X_1-\delta X_1)^2+X_2^2},\quad \theta_{i+1}=\tan^{-1}\frac{X_2}{X_1-\delta X_1} \quad (6)$$

The overdeterministic least-squares analysis [34] was carried out and mixed-mode stress intensity factors were extracted.

Equation (3) is used for a dynamically loaded stationary crack as well for a propagating crack under the following assumptions: The inertial effects enter the coefficients (A_n, B_n, C_n, and D_n)while retaining the functional form of the quasistatic counterpart. The velocity dependent terms were assumed to be small. It has been verified [8] that the contribution from the functions associated with the instantaneous crack-tip velocity is about 3% for a steadily propagating crack with a crack speed of $\sim$300 m/s. The crack-tip transient effects, namely, the rate of change of SIFs and crack accelerations/decelerations, were also small in the current experiments as identified in Ref. [9]. It should be noted that Eq. (3) used in the current work does not account for the spatial variation of mass density in FGM. There are difficulties associated with utilizing the earlier FGM crack-tip fields (which take into account spatial variation of modulus as well as mass density) to analyze the optical interferograms of the current work. The derivations [4,5] describe the spatial variation of elastic modulus and mass density with a single nonhomogeneity parameter in an exponential type of variation or assume mass density to be a constant. However, the glass-filled epoxy FGM used in the current experiments had significantly different elastic moduli and mass density variations. The elastic modulus varied 2.5-fold (4.0–10 GPa) over a width of 43 mm, whereas the mass density variation was 1.5-fold (1175–1700 kg/m^3) over the same length.

4 Computational Procedure

In this study, a cohesive element is developed (in FORTRAN) and implemented in ABAQUS/STANDARD environment as a user-defined element (UEL). The implicit time integration scheme is used to integrate the equations of motion. Generally, for large problems with material nonlinearities, explicit methods are preferred over implicit methods in view of minimizing the solution cost. However, in the current problem, only mild nonlinearity arises from the TSL. Therefore, using an implicit scheme can be justified considering superior convergence rate of Newton's method in ABAQUS/STANDARD. Also, developing a UEL instead of using the cohesive elements (provided in ABAQUS 6.5) gives an added flexibility of applying spatially varying cohesive properties for FGM.

4.1 Cohesive Element Formulation. Let A and B be two coincident material points on a prospective crack path at the time of impact ($t=0$) (see Fig. 6(a)). With the passage of time, their corresponding positions change to A' and B'. Let Δ_n and Δ_t be the normal and tangential components of separation between A' and B'. Let a cohesive element shown in Fig. 6(b) be present on this potential crack path. Then, the separation in the X- and Y-directions at a Gauss point of the element can be computed from nodal displacements $[U]$ as

$$\begin{bmatrix}U_X\\U_Y\end{bmatrix}=[N][U] \quad (7)$$

where

$$[N]=\begin{bmatrix}N_1&0&N_2&0&-N_2&0&-N_1&0\\0&N_1&0&N_2&0&-N_2&0&-N_1\end{bmatrix}$$

and

$$U=[U_1\ V_1\ U_2\ V_2\ U_3\ V_3\ U_4\ V_4]^T$$

Here, $N_1=(1-\xi)/2$ and $N_2=(1+\xi)/2$ are linear shape functions and $\xi=\pm 1/\sqrt{3}$ is the sampling location. The tangential and normal separations are computed by transforming U_X and U_Y into the local coordinate system of the element as

$$\begin{bmatrix}\Delta_t\\\Delta_n\end{bmatrix}=[Q]\begin{bmatrix}U_X\\U_Y\end{bmatrix}\quad\text{where}\quad[Q]=\begin{bmatrix}\cos\theta&\sin\theta\\-\sin\theta&\cos\theta\end{bmatrix} \quad (8)$$

Then, a nondimensional effective separation parameter λ can be defined as

$$\lambda=\sqrt{\left(\frac{\Delta_n}{\delta_n}\right)^2+\left(\frac{\Delta_t}{\delta_t}\right)^2} \quad (9)$$

Here, δ_t and δ_n are the critical values of tangential and normal separations, respectively. At time $t=0$, λ takes the value of zero. As the cohesive element separates, λ increases in magnitude and attains a value of unity when the separation is complete. The variation of pure normal traction (in the absence of tangential separation, $\Delta_t=0$) with normal separation is shown in Fig. 6(c).

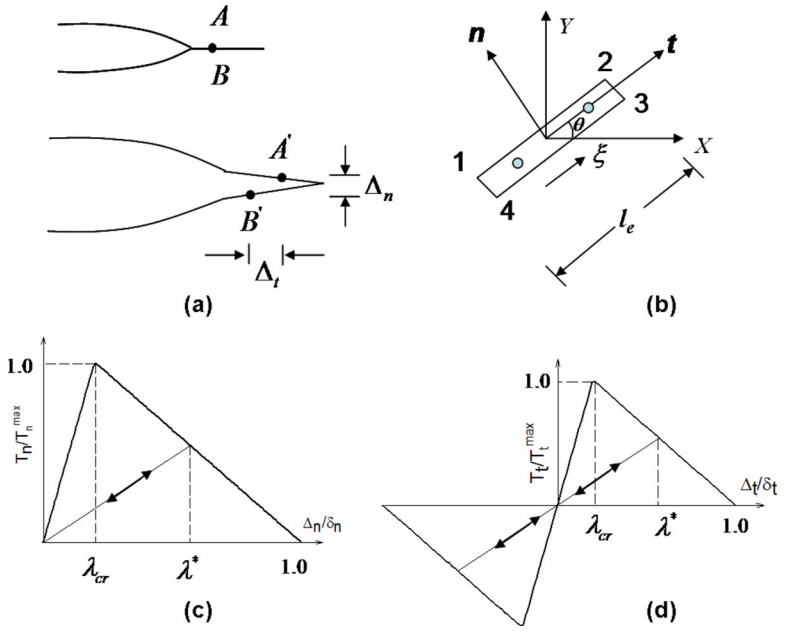

Fig. 6 Details on cohesive element formulations: (*a*) undeformed and deformed configurations of the crack tip region. (*b*) Local and global coordinate systems used for a cohesive element. Prescribed TSL for (*c*) pure normal separation and for (*d*) pure tangential separation.

Similarly, the variation of tangential traction with tangential separation (in the absence of normal separation, $\Delta_n=0$) is shown in Fig. 6(*d*). The critical values of normal and tangential separations are computed by equating the area under T-Δ curves to Mode-I and Mode-II fracture energies,

$$G_{IC} = \tfrac{1}{2}\delta_n T_n^{\max}, \quad G_{IIC} = \tfrac{1}{2}\delta_t T_t^{\max} \tag{10}$$

The traction-separation relations for various portions of the triangular variation are given as follows [24]:

For loading/unloading in the range $0 \leqslant \lambda \leqslant \lambda_{cr}$,

$$T_t = \frac{T_t^{\max}\Delta_t}{\lambda_{cr}\delta_t}, \quad T_n = \frac{T_n^{\max}\Delta_n}{\lambda_{cr}\delta_n} \tag{11}$$

For loading in the range $\lambda_{cr} < \lambda \leqslant 1$,

$$T_t = \frac{T_t^{\max}(1-\lambda)\Delta_t}{\lambda(1-\lambda_{cr})\delta_t}, \quad T_n = \frac{T_n^{\max}(1-\lambda)\Delta_n}{\lambda(1-\lambda_{cr})\delta_n} \tag{12}$$

For unloading/reloading in the range $0 < \lambda \leqslant \lambda^*$ where λ^* is the maximum value of λ after which unloading starts,

$$T_t = \frac{T_t^{\max}\Delta_t}{\lambda^*\delta_t}, \quad T_n = \frac{T_n^{\max}\Delta_n}{\lambda^*\delta_n} \tag{13}$$

For loading in the range $\lambda^* \leqslant \lambda \leqslant 1$,

$$T_t = \frac{T_t^{\max}(1-\lambda)\Delta_t}{\lambda(1-\lambda^*)\delta_t}, \quad T_n = \frac{T_n^{\max}(1-\lambda)\Delta_n}{\lambda(1-\lambda^*)\delta_n} \tag{14}$$

The stiffness coefficients are determined by differentiating tractions with respect to separations as follows:

$$[SS] = \begin{bmatrix} \partial T_t/\partial\Delta_t & \partial T_t/\partial\Delta_n \\ \partial T_n/\partial\Delta_t & \partial T_n/\partial\Delta_n \end{bmatrix} \tag{15}$$

Subsequently, both element stiffness matrix $[S]^e$ and internal force vector $[P]^e$ are computed by performing usual Gauss-quadrature numerical integration as

$$[S]^e_{8\times 8} = \int_{-1}^{1} [N^T]_{8\times 2}[Q^T]_{2\times 2}[SS]_{2\times 2}[Q]_{2\times 2}[N]_{2\times 8}\frac{l_e}{2}d\xi \tag{16}$$

and

$$[P]^e_{8\times 1} = \int_{\xi=-1}^{1} [N^T]_{8\times 2}[Q]_{2\times 2}[T]_{2\times 1}\frac{l_e}{2}d\xi \tag{17}$$

where l_e denotes the length of a cohesive element. The effect of introducing a UEL to the model during an analysis step is that the element should provide its contribution to the *residual force vector* and the *Jacobian matrix* of the overall system of equations [36]. In the current model, since there are no external forces applied to the cohesive elements, the internal force vector (tractions developed due to separation) as given by Eq. (17) becomes the residual force vector. Also, since there is no mass associated with the cohesive elements, the stiffness matrix given by Eq. (16) becomes the Jacobian matrix. Once these two quantities are computed and passed as arguments to ABAQUS, it internally assembles these to formulate a global system of equations and solution proceeds with an automatic time stepping.

4.2 Implicit Dynamic Scheme and Time Step Control. To integrate the equations of motion, implicit time integration is adopted, which uses the implicit operator of Hilber et al. [37] (see Appendix for details). In Eq. (A1), α_d is the parameter that controls algorithmic damping. In the current work, a value of −0.05 was chosen for α_d. This ensures that numerical dissipation is less than 1% of the total energy, which helps to remove the contribution of high frequency modal components and yet maintain good accuracy in the important lower modes. The implicit time step size has to be small enough to capture the transient effects of the problem. The corresponding stable time step size in an explicit dynamic analysis is the time taken by the dilatational wave to travel through the smallest element in the mesh, which is

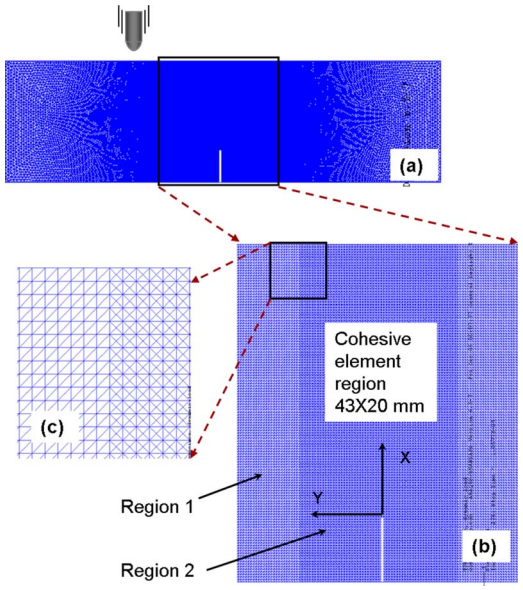

Fig. 7 Finite element discretization. (*a*) Overall view of the finite element discretization, (*b*) magnified view of the mesh showing Region 1 (continuum elements) and Region 2 (continuum and cohesive elements) and (*c*) enlarged view of the mesh near the interface of Regions 1 and 2.

$$\Delta t \leq \frac{L_c}{C_L} \tag{18}$$

where L_c is the smallest continuum element length ($\sim$0.23 mm in the current work) and C_L is the local dilatational wave speed,

$$C_L(X) = \sqrt{\frac{E(X)}{(1+\nu(X))(1-\nu(X))\rho(X)}} \tag{19}$$

for plane stress. Here, $E(X)$, $\nu(X)$, and $\rho(X)$ denote elastic modulus, Poisson's ratio, and mass density of the material at a location X. The maximum value of C_L for the FGM under consideration was 2580 m/s at the stiffer side of the sample. Therefore, the minimum value for Δt is $\sim$90 ns. However, it should be noted that time step size in implicit scheme can be several orders of magnitude greater than the corresponding stable time step size of the explicit scheme. In view of this, the upper limit for time step was set to 200 ns but once the crack initiation occurred, the program internally chose time increments as low as 40 ns.[1]

4.3 Modeling Aspects. The finite element mesh used is shown in Fig. 7(*a*). In mixed-mode dynamic crack growth simulations, the crack path is not known a priori. Therefore, cohesive elements need to be dispersed in a region where crack propagation is anticipated. Hence, the domain was divided into two parts: Region 1 in which crack propagation is not anticipated to occur and Region 2 where crack propagation was observed in experiments (see Fig. 7(*b*)). Accordingly, Region 1 was discretized with three-noded 2D plane stress continuum elements and Region 2 was discretized using three-noded plane stress elements with four-noded cohesive elements dispersed along their boundaries. These two mesh patterns are joined by merging the nodes selectively along their boundaries. The model contained about 117,000 nodes and 125,000 elements.

It is important to make sure that the smallest element size used in the mesh is less than the characteristic cohesive length scale δ so that mesh sensitivity is avoided. This was decided using the size of the cohesive zone based on Dugdale and Barrenblatt's model [15,16] for a Mode-I crack. The cohesive stress assumes a constant value of T_{av} up to a critical opening displacement δ_n and vanishes thereafter. Therefore, the size of the cohesive zone is given by [24,28,38]

$$\delta = \frac{\pi}{8}\frac{E}{1-\nu^2}\frac{G_{IC}}{T_{\text{av}}^2} \tag{20}$$

Here, E is the elastic modulus, G_{IC} is the Mode-I fracture energy, and $T_{\text{av}}=T_n^{\max}/2$, with $T_n^{\max}$ being the peak stress in a bilinear TSL. Minimum value for δ occurs at the stiffer side of the sample and is computed by substituting 10 GPa, 0.49 N/mm, and 100 MPa for E, G_{IC} (both measured under dynamic loading conditions), and $T_n^{\max}$, respectively. The value for δ so obtained is $\sim$845 μm. The smallest cohesive element size chosen in this work is $\sim$230 μm, which is less than one-third of the characteristic cohesive length scale.

While conducting experiments, the FGM samples were initially rested on soft putty blocks before imposing the impact load. This was to preclude support reactions affecting the fracture behavior of the sample. Accordingly, the sample was modeled as a "free-free" beam. The mass of the impactor was large compared to that of the sample. Therefore, a constant velocity of 5 m/s was imposed on the node located at the impact point.

4.4 Application of Graded Material Properties to Continuum Elements. One of the important aspects in finite element modeling of FGM is the implementation of spatially varying material properties. Anlas et al. [39] and Kim and Paulino [40] have developed graded finite elements in order to apply smoothly varying material properties. Rousseau and Tippur [41] used an alternative method to introduce the required spatial variation of material properties using standard elements in any commercial finite element software. Since simulations in the current work are conducted using ABAQUS, it is natural to think of using a user defined material constitutive law (UMAT) to apply spatial variations of material properties as previously done by Giannakopoulos and Suresh [42] under static conditions. However, it should be noted that for dynamic simulations, imposing spatial variation of mass density is also necessary. To our knowledge, currently this is not possible in ABAQUS by using the UMAT option. Therefore, in this work, the method suggested by Rousseau and Tippur [40] was extended to mixed-mode crack growth simulations.

Consider the finite element model shown in Fig. 7(*a*). In the current work, the material properties (elastic modulus, Poisson's ratio, and mass density) were approximated in a linear fashion along the width of the sample before applying to the model. In the first step, an uncoupled thermal analysis was conducted with temperature boundary conditions, $T=T_a$ at the bottom edge and $T=T_b$ at the top edge. No convective boundary conditions were imposed so that temperature variation from T_a to T_b across the width W occurs only through conduction. It should be noted here that as far as the thermal analysis is concerned, the elements in Region 2 (where the cohesive elements are present) are disconnected and no heat flow would occur in this region. In order to overcome this difficulty, first, all the cohesive elements were converted into thermally conductive elements (DGAP in ABAQUS). That is, each four-noded cohesive element was converted into two two-noded DGAP elements. (That is, in Fig. 8(*b*), Nodes 1 and 2 were tied to make first DGAP element and Nodes 3 and 4 were tied to make the next element and so on.) Next, for the DGAP elements, a high value of thermal conductance was assigned. This was to make sure that these elements act as good conductors of heat and both nodes attain the same temperature value. The resulting linear nodal temperature variation following the thermal analysis is shown in Fig. 8(*a*). In the second step, for performing structural analysis using implicit dynamic procedure in ABAQUS/Standard, nodal temperatures from the thermal analysis were im-

[1]The following parameters were used for convergence control [37]: the half-step residual tolerance=20, ratio of the largest residual to the corresponding average force norm (R_n^{α})=0.005, and the ratio of the largest solution correction to the largest corresponding incremental solution value (C_n^{α})=0.01.

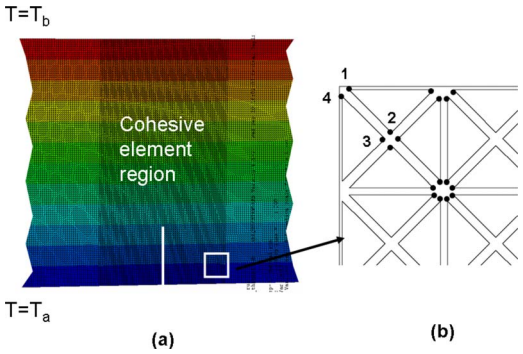

Fig. 8 Thermal analysis to apply graded material properties. (*a*) Nodal temperature results from thermal analysis, and (*b*) magnified view of the cohesive element region.

ported as initial conditions to the model. When nodal temperatures are imposed as boundary conditions, ABAQUS applies them in a ramped fashion over the entire time step and is undesirable. (For a static analysis, however, it does not matter whether temperature field is applied as boundary condition or as an initial condition but for a dynamic analysis, one has to ensure that the nodal temperature values remain the same throughout the time step.) Now, by applying the temperature dependent material properties to the model, a linear variation of elastic modulus and mass density across the sample width W was achieved. Any spurious thermal stresses resulting from the temperature field were avoided by setting thermal expansion coefficient to zero throughout the analysis.

4.5 Application of Material Properties to Cohesive Elements. There are five properties to be specified for cohesive elements. They are Mode-I and Mode-II fracture energies (G_{IC} and G_{IIC}), peak cohesive stresses ($T_n^{\max}$ and $T_t^{\max}$), and the damage parameter corresponding to the peak stress (λ_{cr}). In order to model cohesive elements in FGM realistically, spatial variations of fracture energy and cohesive stress have to be incorporated into the model. The spatial variation of K_{ICR} is available from Fig. 1(*c*) from which G_{IC} ($K_{ICR}^2(x)/E(x)$ for plane stress conditions) can be computed. There is no established physically based rationale for selecting the peak stress $T_n^{\max}$. For example, Xu and Needleman [18] have used $E/10$ in case of polymethyl methacrylate (PMMA), whereas Camacho and Ortiz [27] have used $E/200$ for ceramics. In view of this, several simulations were carried out in the current work by varying the peak stress in the range $E(x)/50$–$E(x)/100$ and the results did not show any significant difference in the crack path. However, the choice of cohesive stress seems to have a modest effect on crack initiation time. For example, when the value of $T_n^{\max}$ was changed from $E/100$ to $E/75$, the crack initiation time changed from 134.2 μs to 130.1 μs. It was desired to keep the value of $T_n^{\max}$ close to the tensile strength of the material which scales roughly by E/100 for the particulate composite used in the current work [43]. Therefore, $T_n^{\max}=T_t^{\max}=E(x)/100$ was chosen for all the simulations. Further more, the ratio of fracture energies and the ratio of peak normal traction to shear traction are also to be selected. It is relatively challenging to perform pure Mode-II experiments under dynamic loading conditions and hence the exact value G_{IIC} is not readily available in literature. Accordingly, a value of $G_{IIC}/G_{IC}=1.0$ was selected in this work. (Additional ratios in the range of $1.0 \leqslant G_{IIC}/G_{IC} \leqslant 3.0$ were attempted but crack path did not show any significant change.)

The variation of K_{ICR} and E over the sample width was approximated by linear functions. Thus, cohesive element properties for the specimen in Fig. 1(*a*) ($E_1 > E_2$) are applied in a linearly decreasing fashion as

$$K_{ICR}(x) = 2.2 - \frac{(2.2-1.4)}{43}x \ (\text{MPa}\sqrt{\text{m}}), \quad 0 \leq x \leq 43 \ \text{nm} \tag{21}$$

and

$$E(x) = 10.0 - \frac{(10.0-4.0)}{43}x \ (\text{GPa}), \quad 0 \leq x \leq 43 \ \text{mm} \tag{22}$$

$$G_{IC}(x) = \frac{K_{ICR}^2(x)}{E(x)}, \quad T_n^{\max}(x) = \frac{E(x)}{100} \quad \text{with}$$
$$G_{IIC}(x) = G_{IC}(x), \quad T_n^{\max}(x) = T_t^{\max}(x) \tag{23}$$

The centroidal location of each cohesive element was calculated and the graded cohesive properties were applied according to Eq. (23). Similarly, for the other configuration ($E_1 < E_2$) where crack is situated on the compliant side of the sample, the properties were applied using linearly increasing functions.

5 Results

The simulations were carried out with material properties applied to continuum and cohesive elements as explained in the previous section. A velocity of 5 m/s was specified to the node located at the impact point.

5.1 Mixed-Mode Stress Intensity Factor Histories. The SIF histories presented in Ref. [9] were based on the assumption that a locally homogeneous material behavior prevails in the crack-tip vicinity in a FGM. However, in the current work, the earlier results were reexamined with the aid of a crack-tip asymptotic expansion that takes into account the local nonhomogeneity. The SIFs were computed by considering a four-term expansion comprising of ($r^{-1/2}$, r^0, $r^{1/2}$, and r^1 terms for stresses, which incorporate the local elastic modulus variation in the sample. The stress intensity factors thus extracted (as explained in Sec. 3) for both configurations are shown in Fig. 9. In this plot, the crack initiation time is denoted by $t_i=0$ so that the positive values correspond to the postinitiation period and the negative ones to the preinitiation period. It should be noted here that SIFs have differences when compared to the ones reported in Ref. [9] since they are evaluated based on the nonhomogeneity parameters α and β (see Eq. (2)). In Fig. 9(*a*), K_I increases monotonically up to crack initiation for both configurations with initiation occurring at $\sim$1.5 MPa m$^{1/2}$. After crack initiation, K_I values show an increasing trend in the case of $E_1 < E_2$ as the crack propagates into a region of increasing reinforcement. However, for the case of $E_1 > E_2$, K_I values somewhat decrease in the observation window after initiation. This difference of K_I histories in the postinitiation region is similar to the one reported by Rousseau and Tippur [8] for the Mode-I case and Kirugulige et al. [1] for syntactic foam based FGMs. It is also confirmed in the finite element simulations to be discussed in the next section. The K_{II} (Fig. 9(*b*)) for both FGM configurations is initially negative and once initiation occurs, K_{II} continues to be a small but negative value for $E_1 < E_2$ whereas it attains a small but positive value for $E_1 > E_2$.

The quality of the least-squares fit (faithfulness of Eq. (5) to represent the surface slopes observed in experiments) is also tested. The synthetic contours generated from Eq. (5) are superimposed on the data points digitized from CGS interferograms and are shown in Figs. 9(*c*) and 9(*d*). One image from the preinitiation and one from the postinitiation period are reported for both FGM configurations. It should be noted here that only the lobes behind the crack tip were digitized while performing overdeterministic least-squares analysis. (The details of the same are available in Ref. [4].) Accordingly, the synthetic contours (order $N=-1$, -1.5, and -2) are superimposed on the data points behind the

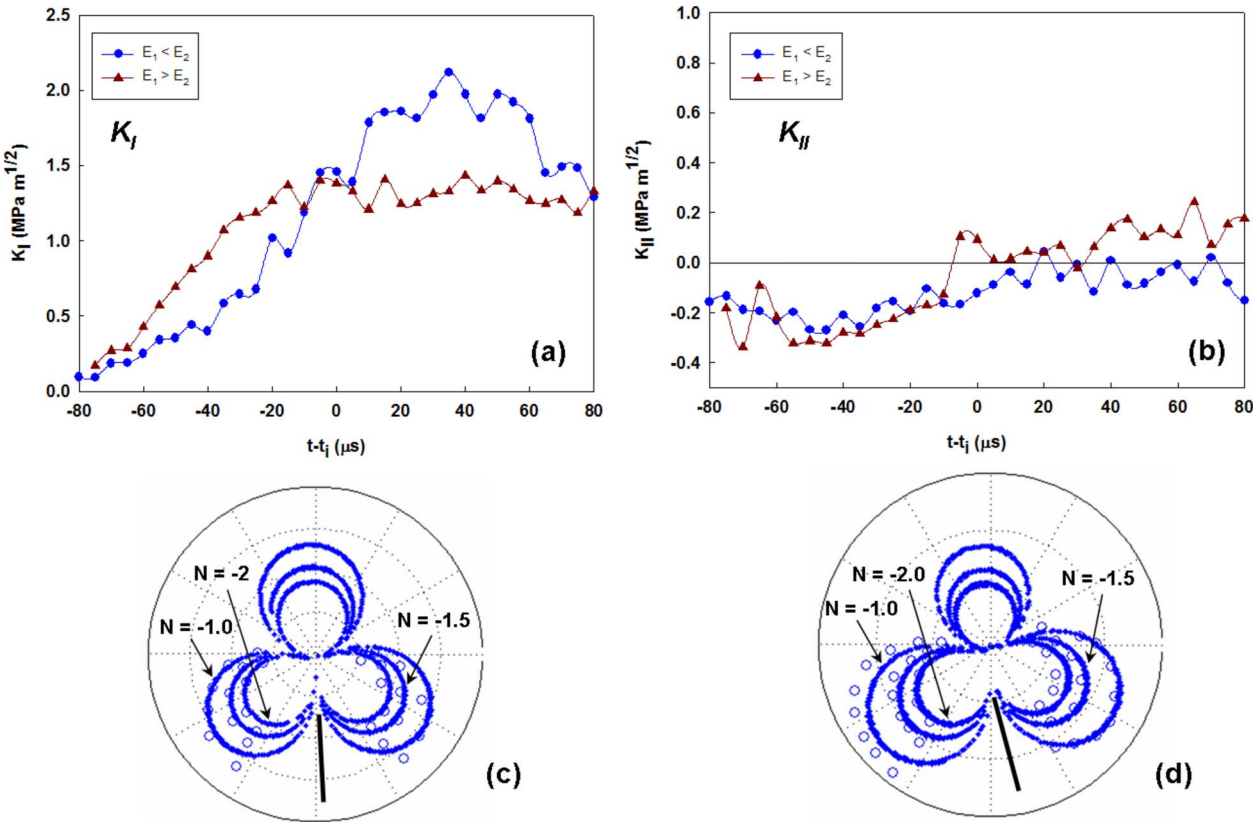

Fig. 9 Stress intensity factors extracted from CGS interferograms by performing overdeterministic least-squares analysis on difference formulation of CGS governing equation (Eq. (5)): (*a*) K_I history and (*b*) K_{II} history. The quality of least-squares fit for (*c*) $E_1 < E_2$ ($t-t_i=20$ μs) and (*d*) $E_1 > E_2$ ($t-t_i=-20$ μs).

crack tip. The least-squares fit considering a four-term FGM solution for the crack-tip stress field shows a good fit with the optical data.

5.2 Energy Computations. Additional insight into the differences in fracture behavior of the two FGM configurations can be obtained by studying the evolution of energy components in finite element simulations. For energy balance, the sum of all the internal energies should to be equal to the external work done on the system. Three types of energies can be identified here; kinetic energy (U_{KE}), strain energy (U_{SE}), and the energy absorbed by the cohesive elements (U_{CE}). The last one consists of two parts; the energy stored in the cohesive elements and the fracture energy. The external work is computed by multiplying impact load with the load point displacement throughout the history (in the current work, since displacement at the impact point is specified, the resulting nodal force is multiplied by the displacement). The energy balance was verified in the simulations for both configurations. Thus, the sum of all the energies (kinetic energy, strain energy, and the energy absorbed by cohesive elements) was found to be equal to the external work up to three significant digits. (For example, in the case of $E_1 < E_2$, at a time of $t=175$ μs, the sum of U_{KE}, U_{SE} and U_{CE} was 248.6286 *N* mm and the external work was 248.6280 *N* mm.) Evolution of U_{KE} and U_{SE} is shown in Fig. 10(*a*). A rapid increase in the kinetic energy for the case of $E_1 < E_2$ is attributed to the motion of denser material in the upper part of the sample. The strain energy is also stored rapidly for this case compared to the $E_1 > E_2$ case since stiffer material is located near the impact point. After about 90 μs for $E_1 < E_2$ and 120 μs for $E_1 > E_2$, the stored strain energy is gradually converted into the fracture energy. The energy absorbed by the cohesive elements is shown in Fig. 10(*b*). Initially, a small portion of the total energy is stored in the cohesive elements, which cause a slow increase of U_{CE} up to 120 μs. An abrupt change in the slope of U_{CE} curves at about 125 μs signifies crack initiation event after which the fracture energy becomes a major portion of U_{CE}. An important observation that can be made from this plot is that more energy is absorbed throughout the loading history by the cohesive elements for the case of $E_1 < E_2$. This can be directly linked to the higher crack speeds observed in experiments as well as in simulations for this configuration.

5.3 Initial Slope of Traction-Separation Law. Cohesive elements are known to introduce undesirable artificial compliance [19,24] into the finite element model. This is especially true when a large number of cohesive elements are dispersed in the model as in the current work. In order to realistically simulate the problem on hand, these artifacts have to be minimized. Therefore, a cohesive law with an initially stiff response was required. The initial slope of the TSL can be changed in the bilinear model rather easily and hence it is used in the current work. Simulations were carried out to study the effects of introducing cohesive elements into the model. The geometry considered for this study was same as the one shown in Fig. 7(*a*) except that *it did not have a crack*. Two beam models were created without a crack, the first one with cohesive elements (in Region 2) and continuum elements (in Region 1), as shown in Fig. 7(*b*). The second model had only continuum elements in Regions 1 and 2 and cohesive elements were absent. The assigned material properties in each case were $E=4.2$ GPa, $\nu=0.34$, and $\rho=1175$ kg/m^3 and the models were loaded with an impact velocity of 5 m/s. Several simulations were conducted (up to 100 μs after impact) by changing the initial slope of the TSL (that is, λ_{cr} was varied in the range 0.05–0.005). The opening displacement, u_y, and stress, σ_y, histories (with respect to the coordinate system shown in Fig. 7(*b*)) were collected at a node located at the midpoint of the lower edge in

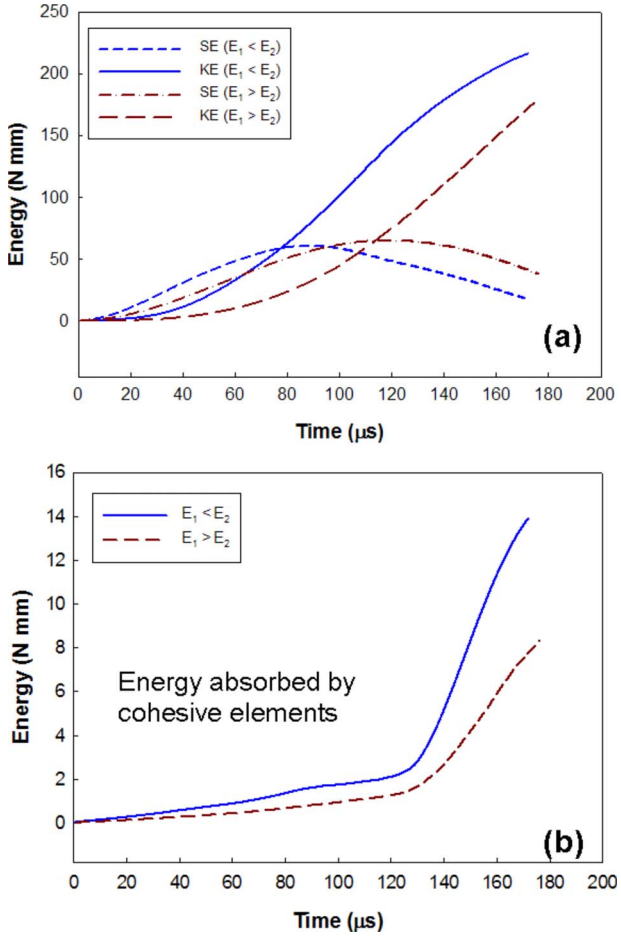

Fig. 10 Evolution of various energies in dynamic simulation for both FGM configurations: (*a*) kinetic energy and strain energy and (*b*) energy absorbed by cohesive elements

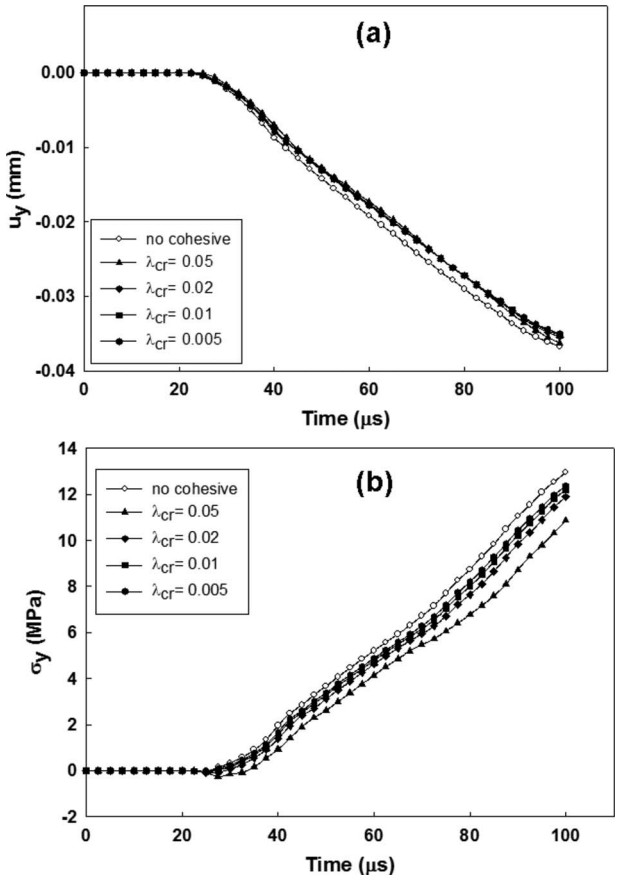

Fig. 11 Effect of the initial slope of the TSL on (*a*) displacement and (*b*) on stress results in elastodynamic simulations on uncracked beams at a node along the lower edge at mid-span

both the models.

The u_y displacement history is shown in Fig. 11(*a*). For an initial duration of 25 μs, there are no noticeable displacements as stress waves have not reached the lower edge of the beam yet. Upon the arrival of stress waves at the bottom edge, u_y monotonically increases up to 100 μs. From Fig. 11(*a*), it can be seen that the effect of introducing cohesive elements on displacements is relatively small. By comparing u_y displacements at 100 μs, a maximum of 4% difference between models without and with the cohesive elements having λ_{cr}=0.005 can be noted. The σ_y history is compared between the two models in Fig. 11(*b*). The effect of artificial compliance, however, can be seen here for larger values of λ_{cr}. For example, when λ_{cr}=0.05, the difference in σ_y between the two models is about 16%. This difference decreases as λ_{cr}. is decreased and stress histories for λ_{cr}=0.005 are rather close to that of the model without any cohesive elements. Also, it should be noted that there seems to be no significant gain in reducing λ_{cr} beyond 0.01 (the difference in σ_y between the two models is 5.8% when λ_{cr}=0.01 and 4.5% when λ_{cr}=0.005). Therefore, a value of λ_{cr}=0.01 was selected throughout this work.

5.4 Crack Path History. Figures 12(*a*) and 12(*b*) show instantaneous cracktip normal stresses before and after crack initiation, respectively, for the case of a crack on the compliant side ($E_1 < E_2$) of the beam. Similar results for the other configuration ($E_1 > E_2$) are shown in Figs. 12(*c*) and 12(*d*). The crack initiation is said to occur in the simulations when the first Gauss point of the first cohesive element is failed. The crack initiation times in simulations are nearly the same for both the configurations (131 μs for $E_1 < E_2$ and 133 μs for $E_1 > E_2$). The similarity in crack paths between experiments and simulations can be seen by comparing Fig. 12(*b*) with Fig. 3(*b*) and Fig. 12(*d*) with Fig. 3(*d*). When the crack is on the compliant side ($E_1 < E_2$), the crack growth trend is close to that of a Mode-I crack (crack kink angle α is ~2.4 deg in simulations whereas ~4 deg in experiments). For the other configuration ($E_1 < E_2$), the kink angle α is ~15 deg in simulations and ~16 deg in experiments. It should be noted here that only a qualitative comparison of crack paths can be made between experiments and simulations because a crack can grow only along element interfaces (in a zigzag fashion) in the model. The stress levels are higher at the beginning of the observation window for $E_1 > E_2$ and the stress contours shrink as the crack grows into a progressively compliant region. The opposite trend is observed for the other configuration where stress levels are lower before initiation and they increase following initiation. Figure 13 shows contour maps of u_y displacements at two instants of time: one before and one after crack initiation. Typical u_y displacement fields for a mixed-mode problem are shown in Figs. 13(*a*) and 13(*c*). As expected, prior to crack initiation, larger displacements occur in case of $E_1 < E_2$ compared to the one with $E_1 > E_2$. From Figs. 13(*b*) and 13(*d*), rapid increase in displacements for $E_1 > E_2$ configuration compared to $E_1 < E_2$ is evident as the crack grows into a progressively compliant material in the former.

The crack length histories from experiments and simulations are plotted in Fig. 14(*a*) and 14(*b*). Here, t_i denotes time at crack initiation. In simulations, cracks initiate at approximately 132 μs in both configurations. This is in contrast to the experimental results shown in Fig. 14(*a*) where the initiation time is in the range 145–155 μs. This difference is attributed to the fact that in ex-

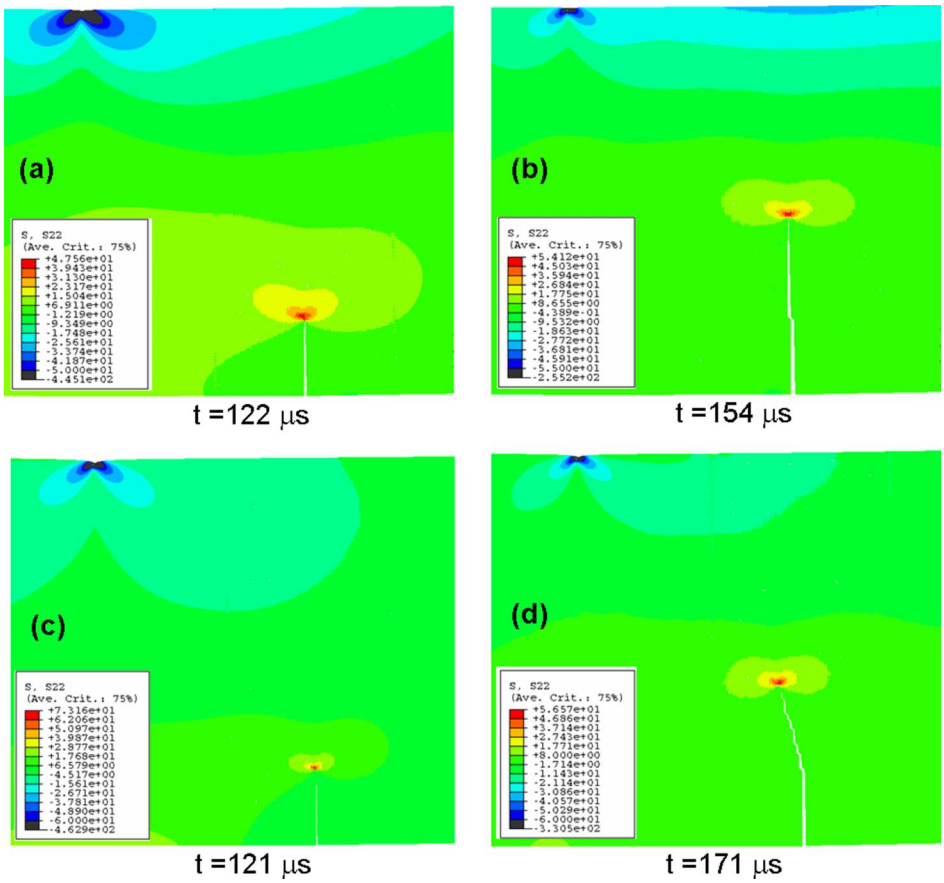

Fig. 12 Snapshots of σ_{yy} stress field at two different time instants: (*a*) 122 μs and (*b*) 154 μs for $E_1 < E_2$ (crack initiation time=131 μs), and (*c*) 121 μs and (*d*) 171 μs for $E_1 > E_2$ (crack initiation time=133 μs)

periments, the initial crack had a finite root radius of ~150 μm whereas in the finite element simulations, it was modeled as a sharp crack. Therefore, more energy had to accumulate at the notch tip before the crack initiated in experiments resulting a delayed response. Furthermore, the crack propagated at higher speeds when it initiated from the compliant side of the model. This agrees well with the experiments (higher slope for $E_1 < E_2$ in Figs. 14(*a*) and 14(*b*)). The higher crack speeds are associated with higher roughness of the fracture surfaces due to the formation of microcracks at the main crack tip resulting in greater energy dissipation.

5.5 *T*-Stress History. In order to understand the marked difference in crack paths for the two configurations, *T*-stress, a measure of in-plane crack tip constraint, was also computed up to crack initiation. Computation of *T*-stress in a mixed-mode dynamic simulation for FGM can be quite challenging. Paulino and Kim [44] have developed a robust and accurate interaction-integral based method to compute *T*-stress in FGM for mixed-mode cracks in the context of finite element simulations. However, in the current work, a modified stress difference method [33] was employed due to the ease of implementation. In this approach, the regression of normal stress difference $(\sigma_x - \sigma_y)$ ahead of the crack tip was used to find the instantaneous *T*-stress as

$$(\sigma_x - \sigma_y)_{\theta=0} = T + Dr \tag{24}$$

where D is the higher order coefficient associated with r^1 term in the asymptotic expansion of $(\sigma_x - \sigma_y)$. It can be seen from Fig. 15(*a*) that $(\sigma_x - \sigma_y)$ has an excellent linearity in the range where a straight line is fitted to the computed data. This process was repeated for all the time steps to get a *T*-stress history in each FGM configuration. The computed *T*-stress histories are plotted in Fig. 15(*b*) up to crack initiation for both configurations. A larger negative *T*-stress is observed for the case of $E_1 < E_2$. This indicates that the crack is likely to grow in its original direction and has lower tendency to kink compared to the other configuration. Similar behavior has been observed by Abanto-Bueno and Lambros [45] for a mixed-mode crack in homogeneous as well as FGM materials.

6 Conclusions

In this investigation, mixed-mode dynamic crack growth behavior in functionally graded glass-filled epoxy sheets is studied, using optical and finite element methods. The experimental study includes mapping deformations in the crack-tip vicinity as a crack initiates and propagates in a mixed-mode fashion in edge cracked FGM beams subjected to one-point impact at an offset distance relative to the initial crack and compositional gradient direction. Angular deflections of light rays proportional to surface slopes in the direction of initial crack orientation are recorded using reflection-mode CGS and high-speed photography. Marked differences in crack paths and crack speeds are observed experimentally. When the crack is initially situated on the compliant side of the beam, the crack growth occurred with a significantly small kink angle when compared to the case when the crack is on the stiffer side with all other experimental parameters being the same. The crack attained higher speeds (by about 100 m/s) in the former case when compared to the latter. The mixed-mode stress intensity factor histories, extracted based on a difference formulation of the crack-tip stress fields with linear variation of materials properties, also show differences. In both cases, the stress inten-

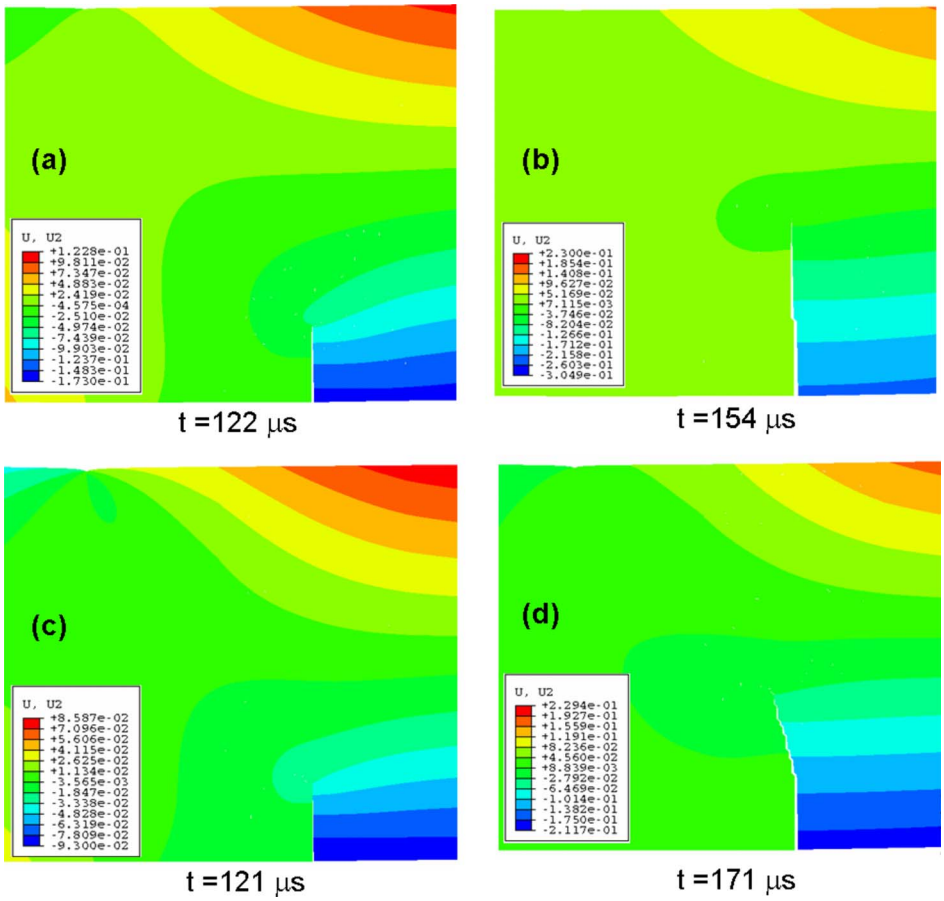

Fig. 13 Snapshots of u_y displacement field at two different time instants: (*a*) 122 μs and (*b*) 154 μs for $E_1 < E_2$ (crack initiation time=131 μs), and (*c*) 121 μs and (*d*) 171 μs for $E_1 > E_2$ (crack initiation time=133 μs)

sity factors increase with a negative (due to a negative K_{II} component) mode mixity up to crack initiation. After crack initiation, increasing Mode-I stress intensity factors accompanied by a small but positive Mode-II component is present in the case with a crack on the stiffer side of the FGM. On the other hand, Mode-I stress intensity factors show little variation after initiation from the compliant side of the FGM but propagate with a small but negative Mode-II component.

In order to understand the differences in crack path and other fracture parameters in the two FGM configurations, finite element simulations are undertaken. An intrinsic cohesive element method with a bilinear TSL was used to model mixed-mode dynamic crack growth. A user subroutine was developed and augmented with ABAQUS™ (Version 6.5) under the option UEL to implement the cohesive elements. The spatial variation of material properties in continuum elements was incorporated by performing a thermal analysis and then applying material properties (elastic properties, Poisson's ratio, and mass density) as temperature dependent quantities. The preinitiation *T*-stress was also computed by a modified stress difference method.

The finite element simulations have successfully captured the dominant characteristics of crack kinking under mixed-mode dynamic loading conditions. The simulated crack paths show a greater kink angle when the crack is on the stiffer side of the FGM. The computed *T*-stress values prior to crack initiation are more negative when the crack is situated on the compliant side of the sample indicating a greater likelihood of a crack to grow in its original direction and has a lower tendency to kink. Also, as in the experiments, higher crack speeds occur when the crack initiates from the compliant side of the FGM. The computed energy histories reveal greater energy dissipation throughout the observation window by the cohesive elements for the case of a crack on the compliant side of the FGM. Since higher crack speeds are accompanied by a greater fracture surface roughness due to microcracking during a dynamic fracture event, this observation is consistent with the higher crack speed seen in experiments when the crack initiates from the compliant side.

Acknowledgment

The authors would like to gratefully acknowledge the support of this research through a grant from the U.S. Army Research Office (Grant No. W911NF-04-10257). Alabama Supercomputer Center (ASC) provided some of the computational facilities for this research. The authors would like to thank the anonymous reviewers for their insightful comments.

Appendix: Direct Integration of Implicit Dynamic Equations

The dynamic equilibrium equations at the end of the current time step $t+\Delta t$ [36,37] is given by

$$M(\ddot{u})_{t+\Delta t} + (1+\alpha_d)\{(R^{\text{int}})_{t+\Delta t} - (R^{\text{ext}})_{t+\Delta t}\} - \alpha_d\{(R^{\text{int}})_t - (R^{\text{ext}})_t\} = 0 \tag{A1}$$

In the above, $\ddot{u}$ is the acceleration field and α_d is a parameter that controls algorithmic damping. Also, M, R^{int}, and R^{ext} are consistent mass matrix, internal force vector, and external force vector, respectively, and are given by

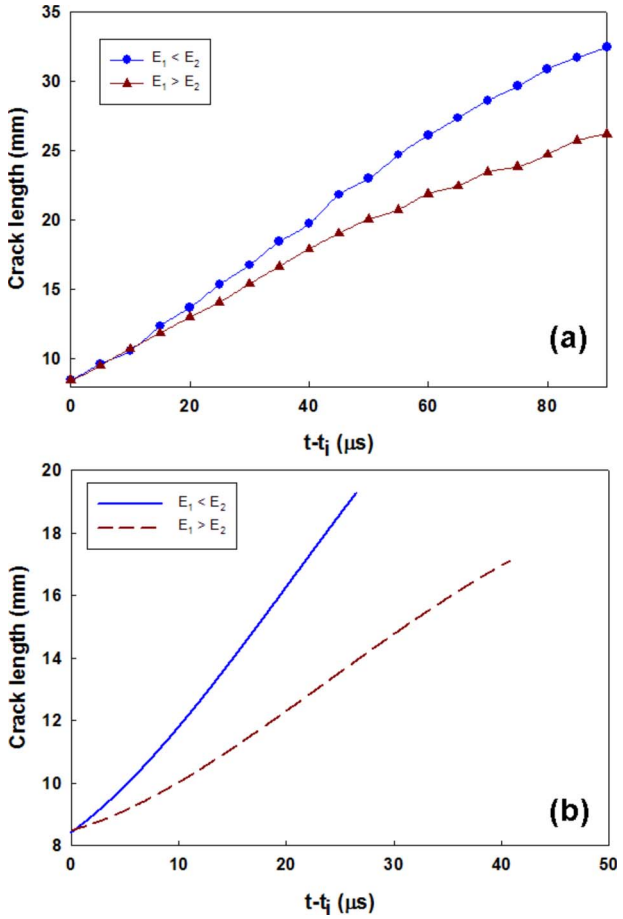

Fig. 14 Crack growth behavior in FGM sample under mixed-mode loading. Absolute crack length history from (*a*) experiments and (*b*) finite element simulations, t_i is crack initiation time (t_i=155 μs for $E_1<E_2$ and 145 μs for $E_1>E_2$ in experiments, and $t_i\sim$130 μs for both $E_1<E_2$ and $E_1>E_2$ in simulations).

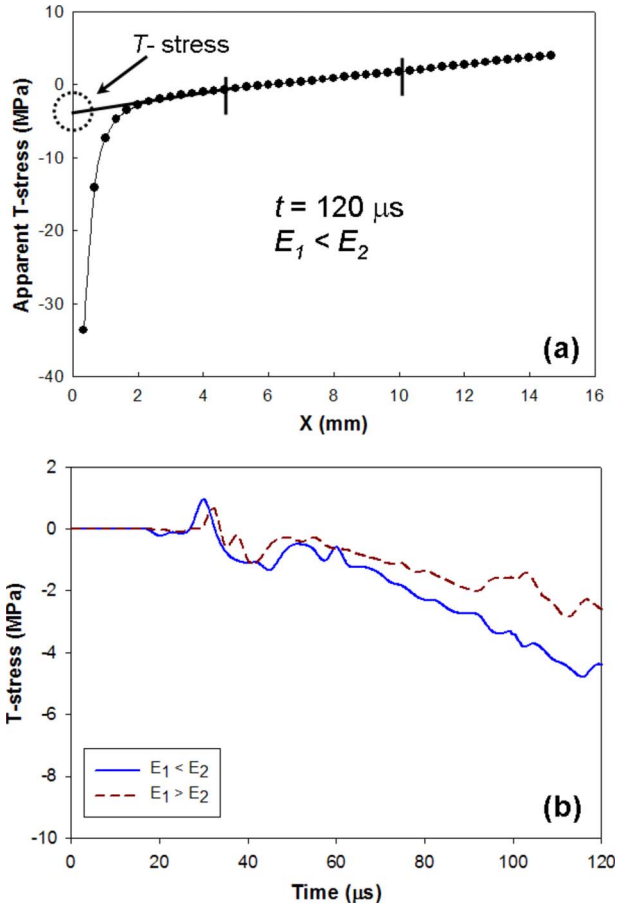

Fig. 15 Nonsingular crack-tip stress histories: (*a*) variation of apparent *T*-stress with radial distance at a certain time instant before crack initiation and (*b*) *T*-stress history up to crack initiation for $E_1<E_2$ and $E_1>E_2$

$$M = \int_{V_0} \rho_0 [N^T][N] dV_0 \tag{A2}$$

$$R^{\text{int}} = \int_{V_0} [B^T][\sigma] dV_0 \tag{A3}$$

and

$$R^{\text{ext}} = \int_S [N^T][T] dS + \int_V [N^T][F] dV \tag{A4}$$

Here, dV and dV_0 are elemental volumes in the current and the reference configurations, respectively, and dS is the current elemental surface area. Furthermore, $[\sigma]$ is the Cauchy stress tensor, $[B]$ is the strain-displacement matrix, and $[N]$ is the matrix of interpolation functions. The quantities $[F]$ and $[T]$ are body force and surface traction force vectors in the current configuration and ρ_0 is the reference mass density. The Newmark formulas for displacement and velocity integrations are as follows:

$$u_{t+\Delta t} = u_t + \Delta t \dot{u}_t + \Delta t^2((\tfrac{1}{2} - \beta_d)\ddot{u}_t + \beta_d \ddot{u}_{t+\Delta t}) \tag{A5}$$

and

$$\dot{u}_{t+\Delta t} = \dot{u}_t + \Delta t((1-\gamma)\ddot{u}_t + \gamma \ddot{u}_{t+\Delta t})$$

$$\beta_d = \tfrac{1}{4}(1-\alpha_d)^2, \quad \gamma_d = \tfrac{1}{2} - \alpha_d, \quad \text{and} \quad -\tfrac{1}{3} \leqslant \alpha_d \leqslant 0 \tag{A6}$$

when α_d=0, β_d and γ_d take the values of $\frac{1}{4}$ and $\frac{1}{2}$, respectively, which is the condition for unconditional stability in an implicit time integration scheme.

References

[1] Kirugulige, M. S., Kitey, R., and Tippur, H. V., 2005, "Dynamic Fracture Behavior of Model Sandwich Structures With Functionally Graded Core: A Feasibility Study," Compos. Sci. Technol., **65**, pp. 1052–1068.

[2] Delale, F., and Erdogan, F., 1983, "The Crack Problem for a Non-Homogeneous Plane," ASME J. Appl. Mech., **50**, pp. 609–614.

[3] Konda, N., and Erdogan, F., 1994, "The Mixed-Mode Crack Problem in a Nonhomogeneous Elastic Medium," Eng. Fract. Mech., **47**(4), pp. 533–545.

[4] Parameswaran, V., and Shukla, A., 1999, "Crack Tip Stress Fields for Dynamic Fracture in Functionally Graded Materials," Mech. Mater., **31**, pp. 579–596.

[5] Chalivendra, V., and Shukla, A., 2005, "Transient Elastodynamic Crack Growth in Functionally Graded Materials," ASME J. Appl. Mech., **72**, pp. 237–248.

[6] Butcher, R. J., Rousseau, C. E., and Tippur, H. V., 1998, "A Functionally Graded Particulate Composite: Preparation, Measurements and Failure Analysis," Acta Mater., **47**(1), pp. 259–268.

[7] Rousseau, C.-E., and Tippur, H. V., 2000, "Compositionally Graded Materials With Cracks Normal to the Elastic Gradient," Acta Mater., **48**, pp. 4021–4033.

[8] Rousseau, C.-E., and Tippur, H. V., 2001, "Dynamic Fracture of Compositionally Graded Materials With Cracks Along the Elastic Gradient: Experiments and Analysis," Mech. Mater., **37**, pp. 403–421.

[9] Kirugulige, M. S., and Tippur, H. V., 2006, "Mixed Mode Dynamic Crack Growth in Functionally Graded Glass-Filled Epoxy," Exp. Mech., **46**(2), pp. 269–281.

[10] Bittencourt, T. N., Wawrzynek, P. A., Ingraffea, A. R., and Sousa, J. L., 1996, "Quasi-Automatic Simulation of Crack Propagation for 2D LEFM Problems," Eng. Fract. Mech., **55**(2), pp. 321–334.

[11] Nishioka, T., 1997, "Computational Dynamic Fracture Mechanics," Int. J.

Fract., **86**, pp. 127–159.
[12] Nishioka, T., Tokudome, H., and Kinoshita, M., 2001, "Dynamic Fracture Path Prediction in Impact Fracture Phenomena Using Moving Finite Element Method Based on Delaunay Automatic Mesh Generation," Int. J. Solids Struct., **38**, pp. 5273–5301.
[13] Kim, J. H., and Paulino, G. H., 2004, "Simulation of Crack Propagation in Functionally Graded Materials Under Mixed-Mode and Non-Proportional Loading," Int. J. Mecha. Mater. Des., **1**, pp. 63–94.
[14] Tilbrook, M. T., Moon, R. J., and Hoffman, M., 2005, "Finite Element Simulations of Crack Propagation in Functionally Graded Materials Under Flexural Loading," Eng. Fract. Mech., **72**, pp. 2444–2467.
[15] Dugdale, D. C., 1960, "Yielding of Steel Sheets Containing Slits," J. Mech. Phys. Solids, **8**, pp. 100–104.
[16] Barenblatt, G. I., 1962, "The Mathematical Theory of Equilibrium Cracks in Brittle Fracture," Adv. Appl. Mech., **7**, pp. 55–129.
[17] Needleman, A., 1987, "A Continuum Model for Void Nucleation by Inclusion Debonding," ASME J. Appl. Mech., **54**, pp. 525–531.
[18] Xu, X. P., and Needleman, A., 1994, "Numerical Simulations of Fast Crack Growth in Brittle Solids," J. Mech. Phys. Solids, **42**(9), pp. 1397–1434.
[19] Wang, Z., and Nakamura, T., 2004, "Simulations of Crack Propagation is Elastic-Plastic Graded Materials," Mech. Mater., **36**, pp. 601–622.
[20] Jin, Z. H., Paulino, G. H., and Dodds, R. H., 2003, "Cohesive Fracture Modeling of Elastic-Plastic Crack Growth in Functionally Graded Materials," Eng. Fract. Mech., **70**(14), pp. 1885–1912.
[21] Shim, D. J., Paulino, G. H., and Dodds, R. H., 2006, "J Resistance Behavior in Functionally Graded Materials Using Cohesive Zone and Modified Boundary Layer Models," Int. J. Fract., **139**(1), pp. 91–117.
[22] Geubelle, P. H., and Baylor, J. S., 1998, "Impact Induced Delamination of Composites: A 2D Simulation," Composites, Part B, **29**, pp. 589–602.
[23] Zavattieri, P. D., Raghuram, P. V., and Espinosa, H. D., 2001, "A Computational Model of Ceramic Microstructures Subjected to Multi-Axial Dynamic Loading," J. Mech. Phys. Solids, **49**, pp. 27–68.
[24] Zhang, Z., and Paulino, G. H., 2005, "Cohesive Zone Modeling of Dynamic Failure in Homogeneous and Functionally Graded Materials," Int. J. Plast., **21**, pp. 1195–1254.
[25] Tvergaard, V., and Hutchinson, J. W., 1994, "The Relation Between Crack Growth Resistance and Fracture Process Parameters in Elastic-Plastic Solids," J. Mech. Phys. Solids, **40**, pp. 1377–1397.
[26] Madhusudhana, K. S., and Narasimhan, R., 2002, "Experimental and Numerical Investigations of Mixed Mode Crack Growth Resistance of a Ductile Adhesive Joint," Eng. Fract. Mech., **69**, pp. 865–883.
[27] Camacho, G. T., and Ortiz, M., 1996, "Computational Modeling of Impact Damage in Brittle Materials," Int. J. Solids Struct., **33**(20–22), pp. 2899–2938.
[28] Ortiz, M., and Pandolfi, A., 1999, "Finite-Deformation Irreversible Cohesive Elements for Three Dimensional Crack Propagation Analysis," Int. J. Numer. Methods Eng., **44**, pp. 1267–1282.
[29] Belytschko, T., and Black, A. T., 1999, "Elastic Crack Growth in Finite Elements With Minimal Re-Meshing," Int. J. Numer. Methods Eng., **45**, pp. 601–620.
[30] Moes, N., and Belytschko, T., 2002, "Extended Finite Elements for Cohesive Crack Growth," Eng. Fract. Mech., **69**, pp. 813–833.
[31] Erdogan, F., and Sih, G. C., 1963, "On the Crack Extension in Plates Under Plane Loading and Transverse Shear," ASME J. Basic Eng., **85D**(4), pp. 519–525.
[32] Dally, J. W., and Sanford, R. J., 1987, "Strain Gage Methods for Measuring the Opening Mode Stress Intensity Factor, K_I," Exp. Mech., **49**, pp. 381–388.
[33] Maleski, M. J., Kirugulige, M. S., and Tippur, H. V., 2004, "A Method for Measuring Mode-I Crack Tip Constraint Under Static and Dynamic Loading Conditions," Exp. Mech., **44**(5), pp. 522–532.
[34] Tippur, H. V., Krishnaswamy, S., and Rosakis, A. J., 1991, "Optical Mapping of Crack Tip Deformations Using the Methods of Transmission and Reflection Coherent Gradient Sensing: A. Study of Crack Tip K-Dominance," Int. J. Fract., **52**, pp. 91–117.
[35] Jain, N., Rousseau, C. E., and Shukla, A., 2004, "Crack Tip Stress Fields in Functionally Graded Materials With Linearly Varying Properties," Theor. Appl. Fract. Mech., **42**, pp. 155–170.
[36] 2004, "Theory and Users Manuals, I, II and III," ABAQUS, Version 6.5, Hibbit, Karlsson and Sorenson, RI.
[37] Hilber, H. M., Hughes, T. J. R., and Taylor, R. L., 1978, "Collocation, Dissipation and Overshoot for Time Integration Schemes in Structural Dynamics," Earthquake Eng. Struct. Dyn., **6**, pp. 99–117.
[38] Rice, J. R., 1968, "Mathematical Analysis in the Mechanics of Fracture," *Fracture, An Advanced Treatise*, Vol. 2, H. Liebowitz, ed., Academic, New York, pp. 191–311.
[39] Anlas, G., Santare, M. H., and Lambros, J., 2000, "Numerical Calculation of Stress Intensity Factors in Functionally Graded Materials," Int. J. Fract., **104**, pp. 131–143.
[40] Kim, J. H., and Paulino, G. H., 2002, "Isoparametric Graded Finite Elements for Nonhomogeneous Isotropic and Orthotropic Materials," ASME J. Appl. Mech., **69**, pp. 502–514.
[41] Rousseau, C.-E., and Tippur, H. V., 2002, "Evaluation of Crack Tip Fields and Stress Intensity Factors in Functionally Graded Elastic Materials: Cracks Parallel to Elastic Gradient," Int. J. Fract., **114**, pp. 87–111.
[42] Giannakopoulos, A. E., and Suresh, S., 1997, "Indentation of Solids With Gradients in Elastic Properties: Part—I. Point Force," Int. J. Solids Struct., **34**, pp. 2357–2392.
[43] Owens, A. T., 2007, "Development of a Split Hopkinson Bar for Testing Stress-Strain Response of Particulate Composites Under High Rates of Loading," MS thesis, Auburn University, Auburn TX.
[44] Paulino, G. H., and Kim, J. H., 2004, "A New Approach to Compute T-Stress in Functionally Graded Materials by Means of Interaction Integral Method," Eng. Fract. Mech., **71**, pp. 1907–1950.
[45] Abanto-Bueno, J., and Lambros, J., 2006, "An Experimental Study of Mixed Mode Crack Initiation and Growth in Functionally Graded Materials," Exp. Mech., **46**, pp. 179–196.